

Solving the three-dimensional Skyrme Hartree-Fock-Bogoliubov problem using the mixed-basis method

Yue Shi (石跃)^{1,*} and Nobuo Hinohara^{2,3}

¹*Department of Physics, Harbin Institute of Technology, Harbin 150001, People's Republic of China*

²*Center for Computational Sciences, University of Tsukuba, Tsukuba 305-8577, Japan*

³*Faculty of Pure and Applied Sciences, University of Tsukuba, Tsukuba 305-8571, Japan*

Background: The symmetry-unrestricted Hartree-Fock-Bogoliubov (HFB) simulation is important for describing various quantum many-body systems. However, the HFB problem in Cartesian coordinate space is numerically challenging.

Purpose: For describing ground states without imposing axial symmetry and looking ahead to future extension for dynamics with full time dependence, we present a numerically efficient implementation of the three-dimensional (3D) HFB code.

Methods: We develop a 3D Skyrme HFB code based on the mixed-basis representation (HFB^{mix}) which consists of two harmonic-oscillator (HO) bases in the x - and y -directions, and finite-difference (FD) basis in the z -direction in solving the nuclear 3D HFB problem.

Results: The results show very well agreement among all the three codes (HFB^{mix}, HO3D, and HFODD). Especially for the HF calculations, the differences in total energies are on the order of a few keV for the lightest O and Mg nuclei. The HFB^{mix} is applied to spherical, prolate, and triaxial systems, and gives the same quadrupole moments for the deformed nuclei as those of the HO-based calculations. Feasibility of the HFB^{mix} is demonstrated in the fission isomer and barrier calculations of ²⁴⁰Pu.

Conclusions: The HFB^{mix} is useful for solving the nuclear 3D HFB problem for its numerical efficiency. Future work will include the analysis of deformed drip-line systems and systematic potential-energy surface calculation for fission-path analysis as well as the time-dependent extension of the HFB^{mix} code for dynamics calculations.

I. INTRODUCTION

For various quantum many-body simulations in quantum chemistry, condensed-matter physics, atomic physics, and nuclear physics, one deals with problems where constituent particles extend far spatially [1]. For example, inside a crystal lattice, the wave functions of the electrons spread extensively within the Coulomb potential exerted by the atomic nuclei which are distributed periodically. Similarly, a composite molecule often constitutes many atoms situated at a significant distance. While the electrons of such a molecule may be localized around a certain atom in the ground state, they may be extended over the whole molecule in the excited states. For some drip-line nuclei where the Fermi energy is close to zero, the dilute nuclear material densities may extend spatially when constituent nucleons occupy orbits with low orbital angular momenta (halo nuclei). In these situations, a microscopic description for the many-body wave functions of the quantum systems *requires* the solution in a three-dimensional (3D) coordinate/momentum space.

In theoretical nuclear physics, a multitude of independent-particle (IP) models play important roles. The conventional IP models use the well-tuned modified harmonic oscillator (HO) or the Woods-Saxon potential plus the spin-orbit (SO) potential to reproduce the experimental magic numbers [2]. Such mean-field models together with the Strutinski shell correction method [3] achieve quantitative success in describing a variety of observables in low-energy nuclear physics. These models are known as microscopic-macroscopic models.

Starting from an effective nucleon-nucleon interaction or Lagrangian together with a variational Hartree-Fock (HF) procedure, one determines the one-body potential in a self-consistent manner [4]. These IP models are known as the self-consistent mean-field theories which are based on the zero-range Skyrme [5, 6] or the finite-range Gogny [7–9] forces, and the relativistic mean-field theory [10–13]. With the advances in synthesizing the exotic nuclei with extreme N/Z ratio, modern self-consistent mean-field theories are more capable of accounting for new features which were not present in nuclei near the valley of stability, such as halo nuclei mentioned above. This *requires* the models to be flexible enough to work in a 3D coordinate space, yet efficient enough for the beyond-mean-field extensions and to cover a large parameter space [4, 14].

However, the requirements are, in general, numerically formidable with the Hartree-Fock-Bogoliubov (HFB) treatment of the pairing correlation. Indeed, in a typical nuclear 3D coordinate-space HFB simulation, one needs to

* corresponding author: yueshi@hit.edu.cn

repeatedly diagonalize the Hamiltonian matrix of the dimension of a few hundreds of thousands [15]. Recent application of the shifted Krylov method [16, 17] and expansion in the three-dimensional wave-number space basis [18] accelerate the 3D symmetry-unrestricted HFB calculations. In comparison, one- [6, 19, 20] or two-dimensional [21–23] HFB calculations in coordinate space are less expensive due to their restricted spatial degrees of freedom.

In realistic applications, one frequently encounters situations where one- or two-dimensional degrees of freedom play a major role in the static or dynamical phenomena which do not possess any spatial symmetry. For example, a fissioning nucleus assumes rather elongated deformation near or beyond the scission point. The inner core of a neutron star may become so dense that the “nuclei” are packed closed to each other with various exotic deformations favoring only one or two spacial degrees of freedom. These are known as the nuclear pasta [24, 25] which have been discussed with various Hartree-Fock calculations in coordinate space [26–28]. In such situations it is more sensible to adopt a coordinate basis in the elongated direction(s) and use HO bases for the remaining directions where the matter is more restricted.

Indeed, a similar idea of using a mixed basis has been realized in the nuclear finite-range Gogny HFB method and its time-dependent extension [29, 30]. The current work intends to describe the implementation of the nuclear Skyrme HFB method using the HO plus finite-difference (HO+FD) mixed basis. Throughout this work, we refer to the basis which consists of the two HO bases in the x - and y -directions, and the FD treatment in the z -direction as the “mixed basis.”

In Sec. II, we describe the nuclear HFB problem and the numerical details for the HO+FD mixed-basis HFB calculation. Section III presents a systematic comparison for the results using the mixed-basis code and those using a 3D HO based code (HO3D) developed in this work and the HFODD codes (version 2.49t) [31]. The summary and perspective are included in Sec. IV.

II. THE MODEL

In this section, we provide a short description of the nuclear HFB theory. We then provide the numerical details for the implementations of the HF(B)^{mix} code and the parameters chosen for the calculations.

A. The Skyrme HFB formalism

In the nuclear Skyrme HF mean-field theory, the total energy E_{Total} of a nucleus can be decomposed into the kinetic, Skyrme, pairing, and Coulomb terms:

$$\begin{aligned} E_{\text{Total}} &= E_{\text{kin+c.m.}} + E_{\text{Skyrme}} + E_{\text{pair}} + E_{\text{Coul}} \\ &= \int d^3r [\mathcal{K}(\mathbf{r}) + \mathcal{E}_{\text{Skyrme}}(\mathbf{r}) \\ &\quad + \mathcal{E}_{\text{pair}}(\mathbf{r}) + \mathcal{E}_{\text{Coul}}(\mathbf{r})]. \end{aligned} \quad (1)$$

The energy densities, $\mathcal{K}(\mathbf{r})$, $\mathcal{E}_{\text{Skyrme}}(\mathbf{r})$, $\mathcal{E}_{\text{pair}}(\mathbf{r})$, and $\mathcal{E}_{\text{Coul}}(\mathbf{r})$, are functionals of various local densities (scalar density ρ , kinetic density τ , spin-current density \mathbf{J} , and pair density $\tilde{\rho}$). The kinetic-energy density of the nucleus with the one-body center-of-mass correction is given by

$$\mathcal{K}(\mathbf{r}) = \frac{\hbar^2}{2m} \tau \left(1 - \frac{1}{A} \right), \quad (2)$$

where m is the nucleon mass and A is the mass number. The time-even part of the Skyrme energy density functional reads

$$\begin{aligned} \mathcal{E}_{\text{Skyrme}}(\mathbf{r}) &= \frac{b_0}{2} \rho^2 - \frac{b'_0}{2} \sum_q \rho_q^2 + b_1 \rho \tau - b'_1 \sum_q \rho_q \tau_q \\ &\quad - \frac{b_2}{2} \rho \nabla^2 \rho + \frac{b'_2}{2} \sum_q \rho_q \nabla^2 \rho_q + \frac{b_3}{3} \rho^{\alpha+2} - \frac{b'_3}{3} \rho^\alpha \sum_q \rho_q^2 \\ &\quad - b_4 \rho \nabla \cdot \mathbf{J} - b'_4 \sum_q \rho_q \nabla \cdot \mathbf{J}_q. \end{aligned} \quad (3)$$

The index q denotes neutrons (n) or protons (p). The local densities without the index q indicate the sum of neutron and proton densities. The current work assumes the time-reversal symmetry and discusses only even-even systems.

Therefore, the time-odd part of the energy density functional does not contribute in Eq. (3). The Coulomb energy is decomposed into the direct and exchange terms

$$\mathcal{E}_{\text{Coul}}(\mathbf{r}) = \mathcal{E}_{\text{Coul}}^{\text{Dir.}}(\mathbf{r}) + \mathcal{E}_{\text{Coul}}^{\text{Exc.}}(\mathbf{r}), \quad (4)$$

where the direct term is given by

$$\mathcal{E}_{\text{Coul}}^{\text{Dir.}}(\mathbf{r}) = \frac{e^2}{2} \int d^3r' \frac{\rho_p(\mathbf{r})\rho_p(\mathbf{r}')}{|\mathbf{r} - \mathbf{r}'|}, \quad (5)$$

and the exchange term is treated in the Slater approximation as

$$\mathcal{E}_{\text{Coul}}^{\text{Exc.}}(\mathbf{r}) = -\frac{3e^2}{4} \left(\frac{3}{\pi}\right)^{1/3} \rho_p^{4/3}(\mathbf{r}). \quad (6)$$

The volume-type pairing energy density is

$$\mathcal{E}_{\text{pair}}(\mathbf{r}) = \sum_q \frac{V_0^q}{4} \tilde{\rho}_q^2(\mathbf{r}). \quad (7)$$

The various local densities are constructed using the quasi-particle wave functions that are solutions of the HFB equation [2, 6]

$$\begin{pmatrix} h_{\uparrow\uparrow} - \lambda & h_{\uparrow\downarrow} & \tilde{h}_{\uparrow\uparrow} & \tilde{h}_{\uparrow\downarrow} \\ h_{\downarrow\uparrow} & h_{\downarrow\downarrow} - \lambda & \tilde{h}_{\downarrow\uparrow} & \tilde{h}_{\downarrow\downarrow} \\ \tilde{h}_{\uparrow\uparrow} & \tilde{h}_{\uparrow\downarrow} & -h_{\uparrow\uparrow} + \lambda & -h_{\uparrow\downarrow} \\ \tilde{h}_{\downarrow\uparrow} & \tilde{h}_{\downarrow\downarrow} & -h_{\downarrow\uparrow} & -h_{\downarrow\downarrow} + \lambda \end{pmatrix} \begin{pmatrix} u_{\uparrow,k} \\ u_{\downarrow,k} \\ v_{\uparrow,k} \\ v_{\downarrow,k} \end{pmatrix} = E_k \begin{pmatrix} u_{\uparrow,k} \\ u_{\downarrow,k} \\ v_{\uparrow,k} \\ v_{\downarrow,k} \end{pmatrix}, \quad (8)$$

where we have omitted the superscripts, q 's, from all quantities for simplicity. The arrows, \uparrow and \downarrow , denote the nucleon spin $\sigma = 1/2$ and $\sigma = -1/2$, respectively. For the four-component quasi-particle wave functions, we have abbreviated that $u_{\uparrow,k} \equiv u_k(\mathbf{r}\sigma = \frac{1}{2})$, for instance.

In Eq. (8) the particle-hole part of the mean-field Hamiltonian is

$$h_{\sigma\sigma'}^q(\mathbf{r}) = \left[-\nabla \cdot \frac{\hbar^2}{2m_q^*(\mathbf{r})} \nabla + U_q(\mathbf{r}) + U_{\text{Coul}}(\mathbf{r}) \delta_{q,p} \right] \delta_{\sigma\sigma'} - [i\mathbf{B}_q(\mathbf{r}) \cdot (\nabla \times \boldsymbol{\sigma})]_{\sigma\sigma'}, \quad (9)$$

where $\boldsymbol{\sigma}$ is a Pauli matrix. The effective mass is defined through

$$\frac{\hbar^2}{2m_q^*(\mathbf{r})} = \frac{\hbar^2}{2m} + b_1\rho - b'_1\rho_q, \quad (10)$$

and

$$\mathbf{B}_q(\mathbf{r}) = b_4\nabla\rho(\mathbf{r}) + b'_4\nabla\rho_q(\mathbf{r}). \quad (11)$$

The potential due to Skyrme force in Eq. (9) reads

$$\begin{aligned} U_q(\mathbf{r}) &= b_0\rho - b'_0\rho_q + b_1\tau - b'_1\tau_q - b_2\nabla^2\rho + b'_2\nabla^2\rho_q \\ &+ \frac{b_3}{3}(\alpha + 2)\rho^{\alpha+1} - \frac{b'_3}{3} \sum_q (\alpha\rho^{\alpha-1}\rho_q^2 + 2\rho^\alpha\rho_q) \\ &- b_4\nabla \cdot \mathbf{J} - b'_4\nabla \cdot \mathbf{J}_q. \end{aligned} \quad (12)$$

For protons ($q = p$), the Coulomb potential in Eq. (9) is composed of the direct and exchange parts

$$U_{\text{Coul}}(\mathbf{r}) = U_{\text{Coul}}^{\text{Dir.}}(\mathbf{r}) + U_{\text{Coul}}^{\text{Exc.}}(\mathbf{r}), \quad (13)$$

where

$$U_{\text{Coul}}^{\text{Exc.}}(\mathbf{r}) = -e^2 \left(\frac{3}{\pi}\right)^{1/3} [\rho_p(\mathbf{r})]^{1/3}. \quad (14)$$

The direct part of the Coulomb potential is obtained by solving the 3D Poisson equation

$$\nabla^2 U_{\text{Coul}}^{\text{Dir.}}(\mathbf{r}) = -4\pi e^2 \rho_p(\mathbf{r}). \quad (15)$$

For details, see Ref. [32]. Upon obtaining $U_{\text{Coul}}^{\text{Dir.}}$, the direct Coulomb energy density (5) can be calculated through

$$\mathcal{E}_{\text{Coul}}^{\text{Dir.}}(\mathbf{r}) = \frac{1}{2} \rho_p(\mathbf{r}) U_{\text{Coul}}^{\text{Dir.}}(\mathbf{r}). \quad (16)$$

The pairing mean-field Hamiltonian in Eq. (8) reads

$$\tilde{h}_{\sigma\sigma'}^q(\mathbf{r}) = \frac{1}{2} V_0^q \tilde{\rho}_q(\mathbf{r}) \delta_{\sigma\sigma'}. \quad (17)$$

The local densities appearing in Eqs. (2), (3), (5), (6), (7), (9), and (17) are expressed in terms of the quasi-particle wave functions of the HFB equation (8)

$$\begin{aligned} \rho_q(\mathbf{r}) &= \sum_k \sum_{\sigma=\pm\frac{1}{2}} |v_{k,q}(\mathbf{r}\sigma)|^2, \\ \tau_q(\mathbf{r}) &= \sum_k \sum_{\sigma=\pm\frac{1}{2}} |\nabla v_{k,q}(\mathbf{r}\sigma)|^2, \\ \tilde{\rho}_q(\mathbf{r}) &= - \sum_k \sum_{\sigma=\pm\frac{1}{2}} v_{k,q}(\mathbf{r}\sigma) u_{k,q}^*(\mathbf{r}\sigma), \\ \mathbf{J}_q(\mathbf{r}) &= -i \sum_k v_{k,q}^\dagger(\mathbf{r}) (\nabla \times \boldsymbol{\sigma}) v_{k,q}(\mathbf{r}). \end{aligned} \quad (18)$$

When evaluating the spin-current density \mathbf{J}_q on the right hand side of Eq. (18), we assume the form of $v_{k,q}(\mathbf{r}) \equiv \begin{pmatrix} v_{k,q}(\mathbf{r}, \frac{1}{2}) \\ v_{k,q}(\mathbf{r}, -\frac{1}{2}) \end{pmatrix}$. The summations over k are limited to the states within the energy window of $0 < E_k < 60$ MeV. This is to make sure the lowest hole state is included.

In practical calculations, one starts with a set of quasi-particle wave functions [$u_k(\mathbf{r}\sigma)$'s and $v_k(\mathbf{r}\sigma)$'s] calculated assuming a Woods-Saxon potential in Eq. (12). The pairing field (17), which is diagonal in the σ space, is initialized with $\tilde{h}_{\uparrow\uparrow}^q(\mathbf{r}) = \tilde{h}_{\downarrow\downarrow}^q(\mathbf{r}) = -3.0$ MeV for $|\mathbf{r}| \leq R$, and $\tilde{h}_{\uparrow\uparrow}^q(\mathbf{r}) = \tilde{h}_{\downarrow\downarrow}^q(\mathbf{r}) = 0$ for $|\mathbf{r}| > R$, where $R = 1.2A^{1/3}$ fm. The obtained quasi-particle wave functions are inserted into Eq. (18) to calculate the densities. One then assembles various potentials and obtains the HFB matrix [Eq. (8)] in some suitable representation. Diagonalizing it, one obtains the new $u_k(\mathbf{r}\sigma)$'s and $v_k(\mathbf{r}\sigma)$'s. This process is continued until convergence is achieved. To ensure stable convergence, we use linearly mixed densities with 75% of the densities from the last iteration.

The particle-hole [Eqs. (12) and (13)] and pairing [Eq. (17)] potentials are diagonal in the coordinate-space representation. Their matrix forms in the HO and FD basis can be obtained conveniently. In Appendix A, we show how the matrix elements of various densities are calculated in the mixed basis. The kinetic and the SO parts in Eq. (9) contain ∇ and ∇^2 operators, which are not diagonal in the coordinate-space representation. In Appendices B and C, we will give expressions for the kinetic terms and SO terms in the mixed basis, respectively.

B. Constraints

For the constrained calculation, we follow the procedure in Ref. [33]. The essential part of the constrained calculation is to add the following contribution to the single-particle potential (9)

$$C \left(\langle \hat{O} \rangle - \mu \right) \hat{O}, \quad (19)$$

where C is the stiffness coefficient; \hat{O} is the multipole operator in question; μ is changing in each iteration with

$$\mu^{(i+1)} = \mu^{(i)} - 0.02 \left(\langle \hat{O} \rangle^{(i+1)} - \mu_0 \right), \quad (20)$$

where μ_0 is the constraint value at the first iteration. This procedure is similar to the linear constraint method, and turns out to give fairly accurate target constrained values at convergence.

In addition to the principal-axes constraint operators described in the next subsection, for the multipole operators appears in this work, we use the quadrupole and octupole operators:

$$\begin{aligned}\hat{Q}_{20} &= 2\hat{z}^2 - \hat{x}^2 - \hat{y}^2, \\ \hat{Q}_{22} &= \sqrt{3}(\hat{x}^2 - \hat{y}^2), \\ \hat{Q}_{30} &= \hat{r}^3 Y_{30}^*(\hat{\Omega}).\end{aligned}\tag{21}$$

The β_2 and γ deformations which measure the degree of axial and triaxial deformations are defined as

$$\begin{aligned}\beta_2 &= \frac{4\pi}{3AR^2} \sqrt{Q_{20}^2 + Q_{22}^2}, \\ \gamma &= \text{atan } Q_{20}/Q_{22},\end{aligned}$$

where $R = 1.2A^{1/3}$ fm, $Q_{20} = \langle \hat{Q}_{20} \rangle$, and $Q_{22} = \langle \hat{Q}_{22} \rangle$.

C. Numerical details

As noted at the end of Sec. II A, after solving the HFB problem in the mixed basis, one obtains a set of eigenvalues and respective eigenfunctions in the HO+FD mixed-basis representation, $(E_k, u_k^{n_x, n_y, i_z}, v_k^{n_x, n_y, i_z})$, where we have ignored the spin and isospin for simplicity. The superscripts of u and v indicate the fact that they are vectors in the $|n_x n_y i_z\rangle$ space. The eigenvectors in the 3D coordinate space can then be obtained using the following transform

$$u_k(i_x, i_y, i_z) = \sum_{n_x} \sum_{n_y} \psi_{n_x}(x_{i_x}) \psi_{n_y}(y_{i_y}) u_k^{n_x, n_y, i_z},\tag{22}$$

$$v_k(i_x, i_y, i_z) = \sum_{n_x} \sum_{n_y} \psi_{n_x}(x_{i_x}) \psi_{n_y}(y_{i_y}) v_k^{n_x, n_y, i_z},\tag{23}$$

where

$$\mu_{i_\mu} = (i_\mu - 0.5) \times d\mu, \quad \mu = x, y, z.\tag{24}$$

We have used the discretized coordinates i_x, i_y, i_z to mirror the situation in the x and y directions. In Eq. (22), $\psi_n(\mu)$ are the HO basis functions [34]. We will call this representation ‘‘grid basis’’ later.

In the implemented HFB code with the mixed basis we use two numbers to characterize the dimension of the basis $|n_x n_y i_z\rangle$, which are N_{max} and N_z .¹ The HO basis number is determined by requiring $n_x + n_y \leq N_{\text{max}}$. The value of N_z specifies the number of grid points in the z direction. Using this basis, the dimension is $\frac{(N_{\text{max}}+1) \times (N_{\text{max}}+2)}{2} \times N_z \times 2$ for the HF calculations. For HFB calculation, the dimension should be doubled. The spacing between grid points is given by dz . It is clear that N_{max} , N_z , and dz uniquely specify our mixed basis. We always select the value of N_z to make sure the simulating box is large enough so that the neutron density at the edge is smaller than 10^{-5} fm⁻³. We use nine-point formulae for both the first- and second-derivative operators with respect to z which will be detailed in Appendix A. For the HO basis, we use an oscillator constant of

$$b_\mu = \sqrt{\frac{41 \times 0.6}{A^{1/3} \times 20.7355}} \text{ fm}^{-1}, \quad \mu = x, y, z.\tag{25}$$

To minimize the difference when comparing the results from HFB^{mix} with those from HFODD, we will readjust the pairing strengths of HFODD calculations to match the pairing energy [Eq. (7)] of HFB^{mix}. To check consistency of such a procedure between the two calculations, another useful quantity is the average pairing gap, which is defined as

$$\Delta_q = -\frac{1}{2N_q} \int d^3r \sum_{\sigma=\pm\frac{1}{2}} \tilde{h}_{\sigma\sigma}^q(\mathbf{r}) \rho_q(\mathbf{r}),\tag{26}$$

where N_q denotes the proton or neutron number.

¹ For HO3D and HFODD calculations, we also use N_{max} to specify the largest N for the spherical HO basis ($n_x + n_y + n_z \leq N_{\text{max}}$). In some HFODD calculations, we use $N_{\text{max}}^{x,y,z}$ to specify the largest N in the x -, y -, and z -direction of the non-uniform HO basis.

For the Coulomb potential, we solve the Poisson equation with two points outside the simulating box as the boundary condition. In the current work, we adopt the Dirichlet boundary condition. Using very similar choices of boundary conditions and discretization method (FD method) in the z direction, we note a good description of spatial vibrations of nucleus [35].

Ideally, one can impose y -simplex symmetry for the wave functions, rendering a block diagonal structure of the HFB matrix in Eq. (8). However, at large deformation, like the case that will be shown in Sec. III B 4 for the fissioning ^{240}Pu , the broken symmetries are encountered often. To allow for future time-dependent extensions capable of complex simulations at large deformation, the currently implemented mixed-basis HFB problem does not impose any spatial symmetry.

If the initial quasi-particle wave functions possess certain symmetry, for instance reflection symmetry, the iteration procedure will preserve the symmetry (known as the self-consistent symmetry [2]). Due to the self-consistent symmetry, most of our calculations which are started from a set of wave functions conserving parity will continue to conserve parity symmetry. We always make sure that the nucleus' principal axes coincide with the Cartesian system by checking the expectation values of the \hat{x} , \hat{y} , \hat{z} , $\hat{x}\hat{y}$, $\hat{x}\hat{z}$, and $\hat{y}\hat{z}$ operators are close to zero. For instance, the center of mass of the triaxially deformed ground state of ^{110}Mo deviates from the origin by only $\langle x, y, z \rangle < 10^{-13}$ fm at convergence. Thus, except for the calculation of the fissioning path of ^{240}Pu where the parity symmetry is explicitly broken by the \hat{Q}_{30} -constraining term, we do not add constraints to fix the orientation or the center of mass of the nucleus. When the axial octupole moment (Q_{30}) of ^{240}Pu deviates from zero, the dipole moment (with operator \hat{z}) is constrained to be zero in order to prevent the center of mass of the nucleus from moving around.

III. RESULTS AND DISCUSSIONS

The HF results provide perhaps the most suitable testing cases for benchmarking codes using different representations. This is because, in the HF case, the occupied single-particle orbits, which are bound, can be made *identical* for the codes using different representations, whereas in the HFB case, this can hardly be achieved. Indeed, to include all the deep-hole states in HFB, one has to include the continuum state in the configuration space. The description of the quasi-particle states in the HFB depends on how the continuum state is discretized in the employed basis representation. This point will be illustrated in Sec. III B. For instance, the HFB calculation for ^{120}Sn with the mixed basis includes 676 proton and 772 neutron quasi-particle states for $0 < E_k < 60$ MeV. In contrast, there are 574 proton and 616 neutron quasi-particle states using the 3D HO basis.

A. HF Results

In this subsection, we perform calculations for two spherical nuclei (^{16}O and ^{208}Pb), one prolately deformed nucleus (^{24}Mg), and one triaxially deformed nucleus (^{64}Ge) using the HF^{mix} code. We compare the results with those of the HFODD code to show the accuracy of the developed mixed-basis code on the HF level. Before evaluating the FD part of the HFB^{mix} code, careful comparisons are made for ^{16}O between HO3D and HFODD codes to check the accuracy of the HO part of the HFB^{mix} code.

1. HO3D v.s. HFODD

Before constructing the HO+FD mixed-basis code, we first implement a 3D HO-basis code, HO3D. This effort is not to have another 3D HO-basis code similar to HFODD, but the HO3D code should be considered as an intermediate byproduct leading to the final mixed-basis code. In this subsection, we first compare the results of HO3D with those of HFODD code. The purpose is to check the implementation of the HO part of the mixed-basis code. In Table I, we list the results of ^{16}O calculated using HO3D and HFODD codes in the same HO model space with $N_{\text{max}} = 14$.

In HO3D, we used the simple trapezoidal rule for the integration over the coordinates in the HO basis. We did not employ the Gauss-Hermite quadrature which is employed in HFODD code, because the basis in the z direction of the mixed-basis code is expressed in the equal-distance grid points, and it is more straightforward to implement the same numerical technique for the integrals and derivatives in x , y , and z directions.

Even with the above-mentioned differences, we see that the agreement between the two codes on the total energy is less than 1 keV for $dz = 0.6$ fm. In an earlier study [32], the HO wave functions are represented in the FD method and the integrals are calculated using the trapezoidal rule. Comparing Table I with Table II of Ref. [32], we observe a similar convergence pattern.

TABLE I. The total energy of ^{16}O and its decomposition into $E_{\text{kin+c.m.}}$, E_{Skyrme} , and E_{Coul} (in MeV) calculated in $N_{\text{max}} = 14$ model space using HFODD and HO3D with different spatial discretizations (dz) for integration. The E_{Skyrme} is further decomposed into E_{ρ^2} , $E_{\rho\tau}$, $E_{\rho^2+\alpha}$, $E_{\rho\nabla^2\rho}$, and E_{SO} which correspond to the space integrals of terms with coefficients (b_0, b'_0), (b_1, b'_1), (b_3, b'_3), (b_2, b'_2), and (b_4, b'_4) in Eq. (3), respectively. Skyrme SLy4 force is employed.

	HO3D ($N_{\text{max}} = 14$)				HFODD
	$dz = 0.9$ fm	$dz = 0.833$ fm	$dz = 0.75$ fm	$dz = 0.6$ fm	($N_{\text{max}} = 14$)
E_{Total}	-128.40483	-128.46119	-128.46798	-128.46573	-128.46614
$E_{\text{kin+c.m.}}$	222.23732	222.16985	222.18856	222.17432	222.18044
E_{ρ^2}	-1304.7338	-1303.3176	-1303.4058	-1303.3125	-1303.3417
$E_{\rho\tau}$	50.50790	50.45808	50.46788	50.46340	50.46476
$E_{\rho^2+\alpha}$	829.76110	828.75045	828.81217	828.74865	828.76895
$E_{\rho\nabla^2\rho}$	61.18723	60.84091	60.83204	60.82523	60.82684
E_{SO}	-0.95678	-0.95063	-0.94971	-0.94994	-0.94962
$E_{\text{Coul}}^{\text{Dir.}}$	16.40879	16.40333	16.40257	16.40072	16.39990
$E_{\text{Coul}}^{\text{Exc.}}$	-2.81656	-2.81562	-2.81571	-2.81562	-2.81566

2. HF^{mix} v.s. HFODD: Spherical nuclei

In Table II we present a set of HF results of ^{16}O using HF^{mix} and HFODD codes. The model space for HFODD is $N_{\text{max}} = 11$, while it is $N_{\text{max}} = 11$ for the HO part of HF^{mix} . Five dz values (1.0, 0.9, 0.833, 0.75, and 0.6 fm) are used to see the convergence property of the code with decreasing grid spacing. For each grid spacings, the N_z values are listed in the table. This corresponds to $z_{\text{max}} = (N_z - 1) \times dz/2 \approx 8$ fm. Because at the edge of the boxes the neutron or proton densities are well below 10^{-6} fm^{-3} , the size of N_z is not the main factor affecting the precision of these calculations.

For the HF^{mix} results, we see a good convergence of the total energy with decreasing dz . For $dz = 0.9$ fm, the total energy overbinds by only < 50 keV compared to the result of $dz = 0.6$ fm. These mixed-basis results show very small quadrupole moments ($Q_{20} < 0.1 \text{ fm}^2$) due to the breaking of the spherical symmetry in the basis. The smallness of the quadrupole deformation calculated for ^{16}O can be considered as a good check for the correctness of the code using a mixed basis. Comparing the HF^{mix} results for ^{16}O with HFODD ones, we notice a good agreement between them. Indeed, the total energy calculated by the HFODD code differs from those of HF^{mix} ($dz = 0.9, 0.833, 0.75$, and 0.6 fm) by only less than 50 keV.

TABLE II. The total energy of ^{16}O and its decomposition into $E_{\text{kin+c.m.}}$, various Skyrme SLy4 energies (defined in Table I), and E_{Coul} as well as the quadrupole moments calculated using HF^{mix} ($N_{\text{max}} = 11$) with different spatial discretizations (dz) and HFODD ($N_{\text{max}} = 11$). All values are in MeV, except for Q_{20} and β_2 which are in fm^2 and dimensionless.

	$\text{HF}^{\text{mix}}(N_{\text{max}} = 11)$					HFODD
	$dz = 1.0$ fm $N_z = 18$	$dz = 0.9$ fm $N_z = 18$	$dz = 0.833$ fm $N_z = 22$	$dz = 0.75$ fm $N_z = 22$	$dz = 0.6$ fm $N_z = 30$	$N_{\text{max}} = 11$
E_{Total}	-128.570	-128.504	-128.490	-128.482	-128.476	-128.450
$E_{\text{kin+c.m.}}$	222.523	222.315	222.276	222.236	222.199	222.348
E_{ρ^2}	-1305.807	-1304.498	-1303.864	-1303.577	-1303.272	-1303.658
$E_{\rho\tau}$	50.614	50.545	50.498	50.478	50.456	-364.383
$E_{\rho^2+\alpha}$	830.487	829.602	829.127	828.920	828.701	828.944
$E_{\rho\nabla^2\rho}$	60.942	60.880	60.825	60.819	60.805	60.809
E_{SO}	-0.931	-0.942	-0.942	-0.946	-0.949	-0.940
$E_{\text{Coul}}^{\text{Dir.}}$	16.418	16.410	16.406	16.403	16.400	16.404
$E_{\text{Coul}}^{\text{Exc.}}$	-2.818	-2.817	-2.816	-2.816	-2.816	-2.817
Q_{20}	0.0238	0.0417	0.0315	0.0713	0.0889	0.0000
β_2	0.0002	0.0004	0.0003	0.0006	0.0008	0.0000

Table III lists the results for the heaviest doubly magic nucleus ^{208}Pb using the HF^{mix} and the HFODD codes. For the HF^{mix} calculations, the integration is performed over the cubic box ($\approx [-12, +12]^3 \text{ fm}^3$). This model space is large enough that the densities at the edges are smaller than 10^{-6} fm^{-3} . The results are shown for $dz = 0.9$ and 0.833 fm with $N_{\text{max}} = 12$ and 14. One can see that the HF^{mix} calculation with $dz = 0.9$ fm provides reasonably converged results, with the energy differences between the two grid spacings being ≈ 50 keV. The total energy calculated with the HF^{mix} is approximately 3 MeV (1 MeV) more bound for $N_{\text{max}} = 12$ (14) than that obtained with the HFODD.

This is due to the limited number of HO bases used. It can be expected that both codes would give closer results when N_{\max} is increased, which is similar to the case of ^{16}O in Table II.

TABLE III. Similar to Table II, but for ^{208}Pb .

	$\text{HF}^{\text{mix}}(N_{\max} = 12)$		HFODD $N_{\max} = 12$	$\text{HF}^{\text{mix}}(N_{\max} = 14)$		HFODD $N_{\max} = 14$
	$dz = 0.9 \text{ fm}$	$dz = 0.833 \text{ fm}$		$dz = 0.9 \text{ fm}$	$dz = 0.833 \text{ fm}$	
	$N_z = 26$	$N_z = 30$		$N_z = 26$	$N_z = 30$	
E_{Total}	-1633.868	-1633.816	-1630.639	-1635.052	-1634.979	-1634.148
$E_{\text{kin+c.m.}}$	3864.117	3863.738	3861.319	3864.062	3863.647	3860.845
E_{ρ^2}	-22378.402	-22375.298	-22359.370	-22376.794	-22373.432	-22359.968
$E_{\rho\tau}$	1330.876	1330.586	1331.301	1329.914	1329.599	1328.865
$E_{\rho^2+\alpha}$	14534.801	14532.581	14523.995	14532.424	14530.027	14521.523
$E_{\rho\nabla^2\rho}$	314.241	314.176	311.518	314.988	314.921	314.602
E_{SO}	-96.053	-96.126	-95.774	-96.174	-96.247	-96.375
$E_{\text{Coul}}^{\text{Dir.}}$	827.807	827.783	827.606	827.789	827.765	827.608
$E_{\text{Coul}}^{\text{Exc.}}$	-31.256	-31.255	-31.233	-31.260	-31.259	-31.248
Q_{20}	6	8	0	-3	-2	0
β_2	0.001	0.001	0.000	0.000	0.000	0.000

Figure 1 plots the neutron density profiles along the three Cartesian directions for the cross sections that are closest to the center of the ^{208}Pb nucleus ($dz = 0.45 \text{ fm}$, $N_{\max} = 12$). For instance, the x profile denotes the neutron density with $y = z = 0.45 \text{ fm}$ ($dz = 0.9 \text{ fm}$), which is the closest point to the center of the nucleus included in the discretization. For this heavy nucleus, one notices rather small difference (The largest difference appears at $z = 1.35 \text{ fm}$, $\Delta\rho \approx 0.0004 \text{ fm}^{-3}$.) between the density profile along z direction and those along the x and y directions. The difference is probably because the density is still converging with increasing N_{\max} in the x and y directions.

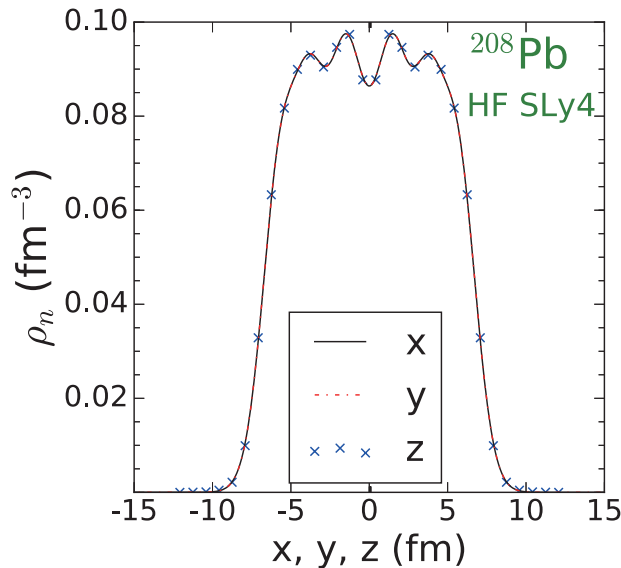


FIG. 1. The neutron density profiles along x , y , and z directions for ^{208}Pb . The density curves of $\rho_n(x, a, a)$, $\rho_n(a, y, a)$, and the discrete points $\rho_n(a, a, z)$ are shown, where $a = 0.45 \text{ fm}$.

In Figure 2, we plot the single-neutron energies for ^{208}Pb using HF^{mix} ($dz = 0.9 \text{ fm}$, $N_{\max} = 12$) and compare them with the results using the HFODD code ($N_{\max} = 12$). We notice good agreement between the two codes. For the HF^{mix} result we see small energy splittings for the single-neutron energies due to the breaking of the spherical symmetry in the basis, whereas the spherical results of HFODD show perfect degeneracy. For the $0h_{9/2}$ levels, the energy splitting in HF^{mix} is about 0.03 MeV. Even in the zoomed-in plot shown in the inset of Fig. 2, the widths are negligible compared to the large gaps which are of a few MeV.

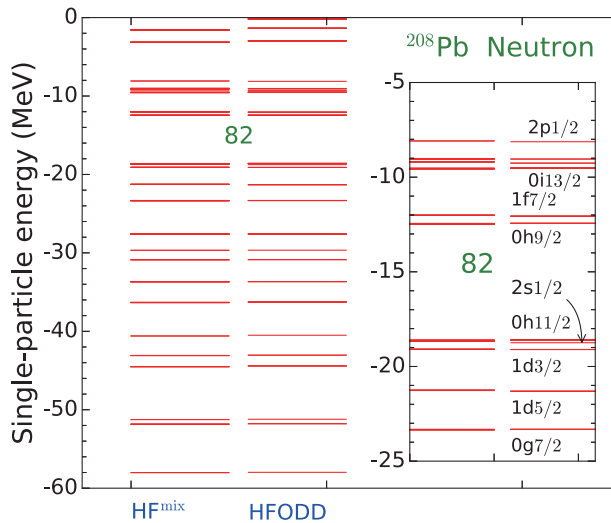


FIG. 2. The single-neutron energies for ^{208}Pb calculated with HF^{mix} and HFODD codes.

3. Prolate nucleus: ^{24}Mg

In Table IV, we present a set of calculations for a light deformed nucleus ^{24}Mg performed for fixed $(N_{\text{max}}, dz, N_z) = (13, 0.833 \text{ fm}, 22)$ and $(13, 0.9 \text{ fm}, 18)$, with z and x being the symmetry axes. It can be seen that the results for both variants agree on the level of a few tens of keV ($\approx 30 \text{ keV}$). Decreasing dz to 0.833 fm results in the absolute binding energies a few tens of keV smaller than those corresponding to $dz = 0.9 \text{ fm}$. Comparing the HF^{mix} results $(N_{\text{max}}, dz) = (13, 0.833 \text{ fm})$ with those of HFODD, we see the agreement is on the order of tens of keV. This better agreement compared to ^{208}Pb might be because the energies have been saturated to the basis-number parameters, N_{max} and dz , for this lighter nucleus. It is satisfying to note that the two codes agree on the calculated β_2 values up to the first two significant digits.

TABLE IV. The calculated energies (in MeV), quadrupole moments (in fm^2), and deformation parameters for ^{24}Mg using the HF^{mix} and HFODD codes. We include results with the symmetry axis of the nucleus being aligned along the z and x directions.

	$N_{\text{max}} = 13, dz = 0.9 \text{ fm}$		$N_{\text{max}} = 13, dz = 0.833 \text{ fm}$		HFODD
	$N_z = 18$		$N_z = 22$		$N_{\text{max}} = 13$
	along z	along x	along z	along x	
E_{Total}	-195.732	-195.698	-195.670	-195.701	-195.660
$E_{\text{kin+c.m.}}$	380.5068	380.539	380.757	380.582	380.462
E_{ρ^2}	-2164.306	-2164.325	-2163.843	-2163.843	-2161.812
$E_{\rho\tau}$	97.389	97.397	97.374	97.352	97.195
$E_{\rho^2+\alpha}$	1395.482	1395.493	1395.401	1395.109	1393.607
$E_{\rho\nabla^2\rho}$	89.039	89.008	88.960	88.946	88.804
E_{SO}	-22.369	-22.335	-22.418	-22.370	-22.389
$E_{\text{Coul}}^{\text{Dir.}}$	32.913	32.914	32.919	32.912	32.903
$E_{\text{Coul}}^{\text{Exc.}}$	-4.388	-4.388	-4.389	-4.388	-4.387
$Q_{20}; Q_{22}$	112; 0	-56; 97	111; 0	-56; 96	112; 0
$\beta_2; \gamma$	0.515; 0°	0.515; 120°	0.510; 0°	0.511; 120°	0.515; 0°

4. Triaxial nucleus: ^{64}Ge

Finally, in Table V we list the calculated energies and quadrupole moments for the triaxially deformed ground states of ^{64}Ge , using the HF^{mix} and HFODD codes. For both variants, we use $N_{\text{max}} = 10$ and 12 . For fixed N_{max} , decreasing dz from 0.9 fm to 0.83 fm results in a $\approx 40 \text{ keV}$ less absolute binding energy. For $N_{\text{max}} = 10$, the total energy of HF^{mix} is $\approx 1.2 \text{ MeV}$ more bound compared to that of HFODD ($N_{\text{max}} = 10$). Increasing N_{max} to 12 results in the difference of total energies between HF^{mix} and HFODD being only $\approx 0.5 \text{ MeV}$. The difference is expected to

decrease with increasing N_{\max} . Again, the calculated β_2 and γ for this medium-heavy triaxial nucleus, are almost identical for all the variants of the calculations.

TABLE V. Similar to Table III, but for ^{64}Ge .

	HF ^{mix} ($N_{\max} = 10$)		HFODD $N_{\max} = 10$	HF ^{mix} ($N_{\max} = 12$)		HFODD $N_{\max} = 12$
	$dz = 0.9$ fm	$dz = 0.83$ fm		$dz = 0.9$ fm	$dz = 0.83$ fm	
	$N_z = 22$	$N_z = 26$		$N_z = 22$	$N_z = 26$	
E_{Total}	-542.795	-542.756	-541.610	-543.086	-543.045	-542.564
$E_{\text{kin+c.m.}}$	1107.085	1106.908	1107.583	1107.070	1106.877	1107.151
E_{ρ^2}	-6571.053	-6569.677	-6568.314	-6569.662	-6568.087	-6570.121
$E_{\rho\tau}$	339.740	339.635	339.847	339.471	339.354	339.788
$E_{\rho^2+\alpha}$	4296.263	4295.267	4294.664	4294.943	4293.799	4295.701
$E_{\rho\nabla^2\rho}$	159.256	159.221	158.793	159.143	159.089	159.172
E_{SO}	-39.230	-39.234	-39.387	-39.176	-39.182	-39.411
$E_{\text{Coul}}^{\text{Dir.}}$	177.485	177.465	177.550	177.465	177.444	177.499
$E_{\text{Coul}}^{\text{Exc.}}$	-12.342	-12.340	-12.347	-12.341	-12.339	-12.342
$Q_{20}; Q_{22}$	259; 135	259; 135	258; 135	258; 136	258; 136	255; 135
$\beta_2; \gamma$	0.262; 28°	0.262; 28°	0.261; 28°	0.261; 28°	0.261; 28°	0.259; 28°

B. HFB Results

In this section, we present the calculated HFB results for one spherical nucleus (^{120}Sn), one prolately deformed nucleus (^{34}Mg), one triaxially deformed nucleus (^{110}Mo) using the HF^{mix} code. We compare them with those calculated using the HFODD code. In addition, we include HF^{mix} results for the typical configurations on the fission path of ^{240}Pu .

1. Spherical nucleus: ^{120}Sn

Table VI lists the results of the HFB calculations for ^{120}Sn using the HF^{mix} and HFODD codes. The same N_{\max} is used for both calculations. The neutron pairing strength V_0^n is set to -200.0 MeV fm³. In HFODD, the results with a reduced neutron pairing strength that provides a similar neutron pairing energy to HF^{mix} are also shown. The total energy for ^{120}Sn of HF^{mix} is ≈ 2 MeV lower than that of the HFODD calculation. This may be due to the relatively small N_{\max} (and large dz) used and the different ways of discretizing the continuum for HF^{mix} and HFODD.

Figure 3 plots the occupation probabilities

$$v_{k,q}^2 = \sum_{\sigma=\pm\frac{1}{2}} \int d^3r |v_k^q(\mathbf{r}, \sigma)|^2, \quad (27)$$

as a function of the quasi-particle energies for ^{120}Sn , calculated with HF^{mix} ($dz = 1.0$ fm) and HFODD codes ($V_0^n = -194.8$ MeV fm³). We see a nice agreement between the two codes, especially for the occupied deep-hole states. A small deviation of E_k and v_k^2 from a perfect degeneracy of the HF^{mix} calculation can be seen, which is associated with the breaking of the spherical symmetry with the small quadrupole deformation, as can be assessed from Table VI. For those states with v_n^2 's close to zero, we see the HF^{mix} gives much more states inside the $E_k < 60$ MeV window than the HFODD does. This is expected because the two codes discretize the continua for $E_k > -\lambda$ differently.

2. Prolate nucleus: ^{34}Mg

In Table VII, we list the results of the HFB calculations with HF^{mix} ($N_{\max} = 14$, $dz = 1.0$ fm) for ^{34}Mg and compare the results with those of the HFODD code. For the HFODD results we include one column with a deformed HO basis using $(N_{\max}^{x,y}, N_{\max}^z) = (13, 16)$. The last column shows the HFODD results with spherical HO basis $N_{\max} = 14$. For the two HFODD results, the pairing strengths have been adjusted to match the $E_{\text{pair}}^{\text{Dir.}}$ of HF^{mix} calculations.

We see that the total energy calculated using HF^{mix} are lower by < 100 keV compared to those of HFODD. The quadrupole moments are rather close to each other between the three variants, with the differences being $\approx 3\%$. It has

TABLE VI. The calculated energies, Fermi energies, and pairing gaps (in MeV), quadrupole moments (in fm^2), and β_2 for ^{120}Sn using the HFB^{mix} and HFODD codes. The Skyrme SLy4 force is used. The neutron pairing strengths are also listed in the first row, which are in MeV fm^3 .

	HFB ^{mix} ($N_{\text{max}} = 10$)		HFODD	
	$dz = 1.0 \text{ fm}$ $N_z = 22$	$dz = 0.9 \text{ fm}$ $N_z = 22$	$N_{\text{max}} = 10$	
V_0^n	-200.0	-200.0	-194.8	-200.0
E_{Total}	-1017.506	-1017.398	-1015.458	-1015.818
$E_{\text{kin+c.m.}}$	2174.025	2173.8967	2170.700	2174.099
E_{ρ^2}	-12683.665	-12680.942	-12655.007	-12661.993
$E_{\rho\tau}$	717.670	717.416	716.451	717.525
$E_{\rho^2+\alpha}$	8264.085	8261.9656	8244.251	8249.274
$E_{\rho\nabla^2\rho}$	224.724	224.619	222.092	222.655
E_{SO}	-49.251	-49.284	-48.554	-49.914
$E_{\text{Coul}}^{\text{Dir.}}$	366.623	366.592	366.375	366.414
$E_{\text{Coul}}^{\text{Exc.}}$	-19.104	-19.103	-19.083	-19.085
$E_{\text{pair}}^{\text{n}}$	-12.614	-12.559	-12.682	-14.793
λ_{n}	-7.974	-7.972	-7.959	-7.951
Δ_{n}	1.436	1.433	1.434	1.572
Q_{20}	7	-1	0	0
β_2	0.002	-0.0003	0.0	0.0

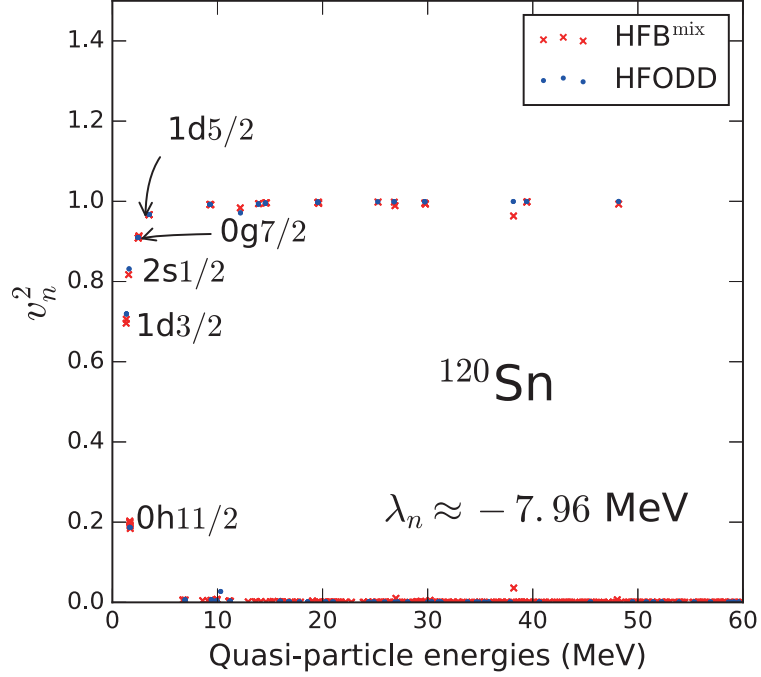


FIG. 3. The calculated occupation probabilities v_n^2 's against the quasi-particle energies for ^{120}Sn .

to be noted that the ground-state quadrupole moment of this nucleus depends on the pairing strengths sensitively. The good agreement between the three variants is thus rather satisfactory. As the pairing strengths of the HFODD results are readjusted to give similar $E_{\text{pair}}^{\text{n,p}}$, the extracted averaged pairing gaps are also close between the two codes.

3. Triaxial nucleus: ^{110}Mo

Table VIII lists the calculated ground states of ^{110}Mo using the HFB^{mix} and HFODD codes ($N_{\text{max}} = 9$) with SkM* force [36]. For HFB^{mix}, we included results with two orientations where the longest axes of the nucleus coincide with the z ($z > x > y$) and x ($x > y > z$) axes. For these HFB^{mix} runs, the dimension of the HFB matrix [Eq. (8)] is

TABLE VII. The calculated energies (in MeV), pairing gaps (in MeV), and quadrupole moments (in fm²) together with the pairing strengths (in MeV fm³) for ³⁴Mg using HFB^{mix} and HFODD codes.

	HFB ^{mix} ($N_{\max} = 14$)		HFODD	
	$dz = 1.0$ fm, $N_z = 18$		$(N_{\max}^{x,y}, N_{\max}^z) = (13, 16)$	$N_{\max}^{x,y,z} = 14$
$V_0^n; V_0^p$	-218.5; -218.5		-217.5; -204.0	-218.5; -205.0
E_{Total}	-257.531		-257.471	-257.479
$E_{\text{kin+c.m.}}$	557.036		557.070	556.983
E_{Skyrme}	-835.730		-835.681	-835.614
$E_{\text{Coul}}^{\text{Dir.}}$	31.752		31.733	31.733
$E_{\text{Coul}}^{\text{Exc.}}$	-4.217		-4.217	-4.217
E_{pair}^n	-3.870		-3.905	-3.883
E_{pair}^p	-2.501		-2.472	-2.480
λ_n	-3.221		-3.258	-3.260
λ_p	-20.126		-20.121	-20.112
Δ_n	1.325		1.328	1.328
Δ_p	1.262		1.213	1.215
Q_{20}	99		102	102
β_2	0.255		0.262	0.262

4840. Each iteration takes about 20 min to finish on Intel(R) Xeon(R) CPU E5-2697 v4 processor.

The total energy obtained with $z > x > y$ is about 0.6 MeV lower than the result with the longest axis in the x direction. This is because the z direction is treated with the FD method allowing for better description of the spatially extended density compared to the HO basis. It is very interesting to note that the β_2 values of all the calculated triaxial ground states differ only from the third significant digits.

TABLE VIII. The calculated energies, pairing gaps (in MeV), and total quadrupole moments (in fm²) of ¹¹⁰Mo calculated with HFB^{mix} and HFODD codes. The Skyrme force used is SkM*. The neutron pairing strengths are also shown in unit of MeV fm³, and for the proton pairing strength we use $V_0^p = -170.0$ MeV fm³. The calculated nucleus is placed in the principal axis, where $z > x > y$ indicates that the longest, medium, and shortest axes of the nucleus are aligned in the z , x , and y directions, respectively. The β_2 and γ deformations are defined in Sec II B.

	HFB ^{mix} ($N_{\max} = 9$, $dz = 1.0$ fm, $N_z = 22$)		HFODD
	$z > x > y$	$x > y > z$	$N_{\max} = 9$
V_0^n	-170.0	-170.0	-172.7
E_{Total}	-920.571	-919.965	-918.532
$E_{\text{kin+c.m.}}$	2010.785	2011.839	2008.9216
E_{ρ^2}	-12268.080	-12265.004	-12235.894
$E_{\rho\tau}$	368.900	368.671	367.849
$E_{\rho^2+\alpha}$	8600.508	8597.598	8575.708
$E_{\rho\nabla^2\rho}$	193.730	192.776	190.496
E_{SO}	-73.691	-73.000	-72.646
$E_{\text{Coul}}^{\text{Dir.}}$	266.902	266.847	266.618
$E_{\text{Coul}}^{\text{Exc.}}$	-15.749	-15.740	-15.718
E_{pair}^n	-3.875	-3.885	-3.867
λ_n	-5.414	-5.407	-5.379
Δ_n	0.762	0.763	0.771
$Q_{20}; Q_{22}$	949; 361	-780; 632	943; 365
$\beta_2; \gamma$	0.369; 21°	0.364; -39°	0.367; 21°

4. Selected Points on the Fission pathway of ²⁴⁰Pu

Finally, in Table IX, we present the calculated results for the fission pathway of ²⁴⁰Pu using HFB^{mix} (SkM*). For this calculation, we use $(N_{\max}, dz, N_z) = (8, 1.2$ fm, 26). The neutron and proton pairing strengths are $V_0^n = V_0^p = -170.0$ MeV fm³. These pairing strengths give reasonable pairing energy for the ground state of ²⁴⁰Pu. We select several configurations along the fission pathway, that is, the results corresponding to the ground state (g.s.), the fission isomer (Fis. Iso.), the first/inner fission barrier (1st Fis. Bar.), the second/outer fission barrier (2nd Fis.

Bar.), and one deformation point beyond the second fission barrier at $Q_{20} = 150$ b. Here, we have assumed that the fission pathway is described in the space spanned by the several multipole deformations. Ideally, one should obtain the solutions corresponding to the barriers by calculating the full potential energy surface before the scission area. However, due to the limitation of the computational resources, we restrict our search within the points near the two fission barriers. For example, to find the first fission barrier, we perform calculations with Q_{20} being constrained from 50 to 70 b at a step of 5 b. We do not impose axial nor reflection symmetries; we allow Q_{22} and Q_{30} to vary freely when Q_{20} is constrained. The important deformations which lower the fission barrier and the information on the barrier position in the potential energy surface in the case of SkM* functional are known from the literature such as Ref. [37].

TABLE IX. The calculated energies (in MeV), pairing gaps (in MeV), quadrupole moments [in barn (b)], and octupole moment (in $b^{3/2}$) for selected deformation points on the fission path of ^{240}Pu using HFB^{mix} (SkM* force).

	g.s.	Fis. Iso.	1st Fis. Bar.	2nd Fis. Bar.	
E_{Total}	-1794.741	-1792.300	-1787.055	-1788.195	-1790.132
$E_{\text{kin+c.m.}}$	4447.739	4441.681	4442.885	4427.123	4431.331
E_{Skyrme}	-7230.115	-7186.925	-7192.441	-7135.954	-7118.399
$E_{\text{Coul}}^{\text{Dir.}}$	1025.625	992.332	1006.738	963.173	939.697
$E_{\text{Coul}}^{\text{Exc.}}$	-35.687	-35.603	-35.620	-35.537	-35.540
$E_{\text{pair}}^{\text{n}}$	-1.399	-2.937	-7.532	-6.579	-6.241
$E_{\text{pair}}^{\text{p}}$	-0.904	-0.848	-1.085	-0.652	-0.979
λ_{n}	-6.383	-6.626	-6.257	-6.310	-6.428
λ_{p}	-4.484	-4.715	-4.574	-5.155	-5.180
Δ_{n}	0.318	0.463	0.747	0.687	0.665
Δ_{p}	0.264	0.262	0.297	0.228	0.251
Q_{20}	29.9	83.2	60.6	120.0	150.3
Q_{22}	0	0	8.6	4.9	3.0
Q_{30}	0	0	0	6.1	9.4

The excitation energy of the fission isomer extracted from Table IX is 2.4 MeV; the heights of the inner and outer fission barriers are 7.7 and 6.5 MeV, respectively. Comparing these three energies with those of Ref. [37] calculated with HFODD, we notice that our results are smaller than theirs by ≤ 0.3 MeV. These small deviations can be attributed to the rather small $N_{\text{max}} = 8$ used in our calculations. Another source of discrepancies is the differences in the pairing treatment (both pairing strengths and pairing types chosen).

Figure 4 shows the density profiles of the fission isomer along the three axes. In Table IX we include the calculated results for a deformation beyond the second fission barrier. In the future, the HFB^{mix} code will be extended to allow for the full time-dependent HFB simulation which will be started from a HFB solution corresponding to the deformation point beyond the second fission barrier.

Although the HFB^{mix} is capable of describing the extremely elongated configuration, such as those near or beyond the scission point of the fissioning nucleus, it is not the intention of the current paper to perform the full fission-path calculation of ^{240}Pu . Here we are content to demonstrate the *feasibility* of the HFB^{mix} code for describing some of the typical configurations of ^{240}Pu fission pathway. We leave a more realistic and systematic survey of the potential energy surface for the future project with larger basis size and better pairing treatment.

IV. SUMMARY AND PERSPECTIVE

We solve the numerically demanding three-dimensional (3D) coordinate-space nuclear Hartree-Fock-Bogoliubov (HFB) problem using a mixture of bases, which consist of two harmonic-oscillator (HO) bases in the x and y directions, and one finite-difference basis in the z direction.

We implement the 3D HO and the mixed-basis codes. Using the mixed-basis code, we perform systematic calculations for spherical and deformed nuclei using the Hartree-Fock (HF) and HFB methods. The results obtained are compared with those of the 3D HO-based code, HFODD.

The differences of the total energies using the HF method for lightest nucleus ^{16}O is in the order of a few tens of keV between the two HO-based codes, HO3D and HFODD. For the lightest nuclei, ^{16}O and ^{24}Mg , where the total energies tend to be converged with increasing N_{max} , the total energy differences are only a few tens of keV. For heavier nuclei ($A > 100$), the differences in total energies are about 1-2 MeV. The differences decrease with the increase of the largest N_{max} of the HO bases. Hence, for the heavier nuclei, the difference between mixed-basis code and HFODD can be attributed to the fact that the HF result is still converging with N_{max} .

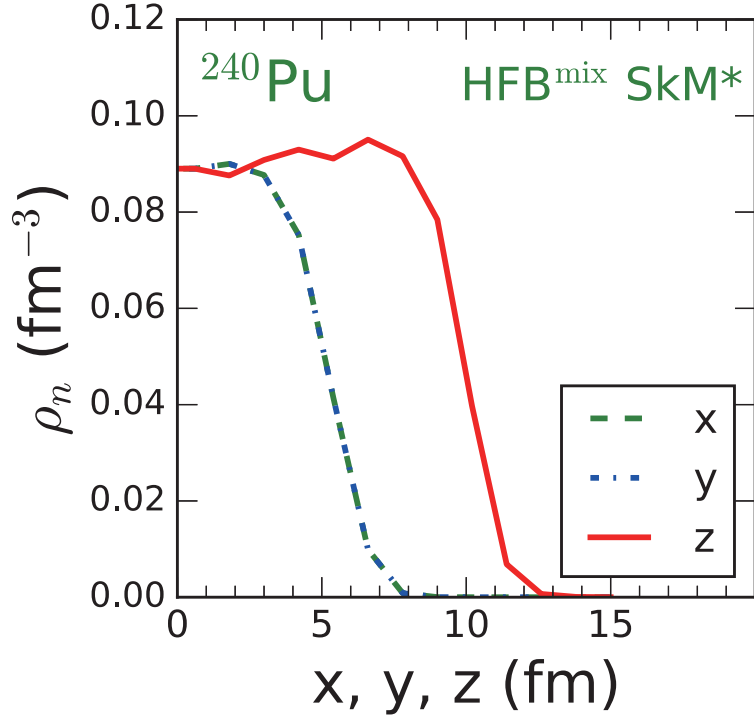


FIG. 4. The density profiles of the fission isomer of ^{240}Pu calculated using HFB^{mix} (Table IX). The density values correspond to the lines with other coordinates closest to the center of the nucleus.

Comparisons of the HFB results using the HFB^{mix} and the HFODD codes show similar convergence behavior with respect to N_{max} as the HF case. Specifically, the differences of the total energies using HFB^{mix} and HFODD decrease with increasing N_{max} .

For spherical nuclei, the calculated quadrupole moments are negligibly small for the mixed-basis HF and HFB codes. For deformed nuclei, the differences in the quadrupole moments calculated using the mixed-basis codes are almost identical to those of the HFODD code. A good agreement of single/quasi-particle energies is also seen between the mixed-basis codes and that of the HFODD code.

As a demonstration of the applicability of the HFB^{mix} code to extremely elongated deformations, selected configurations along the fission pathway in ^{240}Pu are calculated. With future optimizations of the code, the HFB^{mix} will be advantageous in a systematic survey of the potential energy surfaces with elongated configurations as well as the deformed drip-line nuclei.

Our future work will be focused on the time-dependent extension of the current mixed-basis HFB method. Such a mixed-basis strategy would make the full 3D time-dependent HFB calculations much more affordable and flexible.

ACKNOWLEDGMENTS

The current work is supported by National Natural Science Foundation of China (Grant No. 12075068 and No. 11705038), the Fundamental Research Funds for the Central Universities (Grant No. HIT.BRET.2021003), JSPS KAKENHI Grant No. 16K17680 and No. 20K03964, and the JSPS-NSFC Bilateral Program for the Joint Research Project on “Nuclear mass and life for unravelling mysteries of r-process.” YS thanks the HPC Studio at Physics Department of Harbin Institute of Technology for computing resources allocated through INSPUR-HPC@PHY.HIT.

Appendix A: The densities in the mixed basis

In this section, we specifically provide the detailed formulae of various densities [Eq. (18)] using the mixed basis. To compute the densities, τ , $\nabla \cdot \mathbf{J}$, and $\nabla \rho$, which are needed for the construction of the potentials and mean-field

Hamiltonian, one needs the following first derivatives

$$\frac{\partial}{\partial x} v_k(x_{i_x}, y_{i_y}, z_{i_z}) = \sum_{n_x} \sum_{n_y} \psi'_{n_x}(x_{i_x}) \psi_{n_y}(y_{i_y}) v_k^{n_x, n_y, i_z}, \quad (\text{A1})$$

$$\frac{\partial}{\partial y} v_k(x_{i_x}, y_{i_y}, z_{i_z}) = \sum_{n_x} \sum_{n_y} \psi_{n_x}(x_{i_x}) \psi'_{n_y}(y_{i_y}) v_k^{n_x, n_y, i_z}, \quad (\text{A2})$$

$$\frac{\partial}{\partial z} v_k(x_{i_x}, y_{i_y}, z_{i_z}) = \sum_{n_x} \sum_{n_y} \psi_{n_x}(x_{i_x}) \psi_{n_y}(y_{i_y}) \sum_{d=-\lambda}^{+\lambda} m_d^{(1)} v_k^{n_x, n_y, i_z+d}, \quad (\text{A3})$$

where the $m_d^{(1)}$ is the FD coefficients for the first derivative. For the nine-point FD case ($\lambda = 4$), the coefficients for the first ($m_d^{(1)}$) and second ($m_d^{(2)}$) derivatives are listed in Table X. These are used throughout this work.

TABLE X. The nine-point FD weights of the first and second derivatives.

d	-4	-3	-2	-1	0	1	2	3	4
$m_d^{(1)}$	$\frac{1}{280}$	$-\frac{4}{105}$	$\frac{21}{105}$	$-\frac{84}{105}$	0	$\frac{84}{105}$	$-\frac{21}{105}$	$\frac{4}{105}$	$-\frac{1}{280}$
$m_d^{(2)}$	$-\frac{1}{560}$	$\frac{8}{315}$	$-\frac{1}{5}$	$\frac{8}{5}$	$-\frac{205}{72}$	$\frac{8}{5}$	$-\frac{1}{5}$	$\frac{8}{315}$	$-\frac{1}{560}$

As for the term involving Laplacian ($\nabla^2 \rho$), one needs $\nabla^2 v_k$. This can be done in a similar manner as Eqs. (A1) - (A3),

$$\frac{\partial^2}{\partial x^2} v_k(x_{i_x}, y_{i_y}, z_{i_z}) = \sum_{n_x} \sum_{n_y} \psi''_{n_x}(x_{i_x}) \psi_{n_y}(y_{i_y}) v_k^{n_x, n_y, i_z}, \quad (\text{A4})$$

$$\frac{\partial^2}{\partial y^2} v_k(x_{i_x}, y_{i_y}, z_{i_z}) = \sum_{n_x} \sum_{n_y} \psi_{n_x}(x_{i_x}) \psi''_{n_y}(y_{i_y}) v_k^{n_x, n_y, i_z}, \quad (\text{A5})$$

$$\frac{\partial^2}{\partial z^2} v_k(x_{i_x}, y_{i_y}, z_{i_z}) = \sum_{n_x} \sum_{n_y} \psi_{n_x}(x_{i_x}) \psi_{n_y}(y_{i_y}) \sum_{d=-\lambda}^{+\lambda} m_d^{(2)} v_k^{n_x, n_y, i_z+d}. \quad (\text{A6})$$

In the case of 3D HO basis, the calculation of gradient and Laplacian of v_k is more straightforward where the z direction is calculated in a similar way as those of the x and y directions.

After obtaining the gradient and the Laplacian of v_k , one assembles the densities [38]

$$\begin{aligned} \rho &= D_{00}^{\uparrow\uparrow} + D_{00}^{\downarrow\downarrow}, \\ \tau &= \sum_{\mu} (D_{\mu\mu}^{\uparrow\uparrow} + D_{\mu\mu}^{\downarrow\downarrow}), \\ \nabla^2 \rho &= 2\Re(L^{\uparrow\uparrow} + L^{\downarrow\downarrow}) + 2\tau, \\ \nabla \cdot \mathbf{J} &= -2\Im(D_{23}^{\uparrow\downarrow} - D_{32}^{\uparrow\downarrow}) \\ &\quad - 2\Re(D_{31}^{\uparrow\downarrow} - D_{13}^{\uparrow\downarrow}) \\ &\quad + 2\Im(D_{21}^{\uparrow\uparrow} - D_{21}^{\downarrow\downarrow}), \\ \nabla_k \rho &= 2\Re(D_{k0}^{\uparrow\uparrow} + D_{k0}^{\downarrow\downarrow}), \quad k = 1, 2, 3, \end{aligned}$$

where

$$D_{\mu\nu}^{\sigma\sigma'} = \sum_k [\nabla_{\mu} v_k(\mathbf{r}\sigma)] [\nabla_{\nu} v_k^*(\mathbf{r}\sigma')], \quad (\text{A7})$$

$$L^{\sigma\sigma'} = \sum_k v_k(\mathbf{r}\sigma) [\nabla^2 v_k^*(\mathbf{r}\sigma')], \quad (\text{A8})$$

and $\nabla_{\mu} \equiv (1, \nabla)$. Using Eqs. (A1) - (A6), one can also obtain the Laplacian of the effective mass in Eq. (B1).

Appendix B: The kinetic terms in HO and mixed bases

In this subsection, we give the matrix elements of the kinetic term in the HO and mixed-basis representations. Before showing the kinetic term in the coordinate representation, one notices that, when applied to a function, the kinetic part of Eq. (9) can be written as [16]

$$\hat{h}^{\text{kin}} \cdot \psi(\mathbf{r}) = -\frac{1}{2} \left\{ \frac{\hbar^2}{2m^*(\mathbf{r})} \nabla^2 \psi(\mathbf{r}) + \nabla^2 \left[\frac{\hbar^2}{2m^*(\mathbf{r})} \psi(\mathbf{r}) \right] - \left(\nabla^2 \frac{\hbar^2}{2m^*(\mathbf{r})} \right) \psi(\mathbf{r}) \right\}. \quad (\text{B1})$$

The matrix element of the third term of right hand side of Eq. (B1) is diagonal in the FD basis.

1. The matrix element of kinetic terms in the 1D grid basis

Next we examine the matrix form of the Laplacian operator ∇^2 in the 1D grid representation. The second derivative of a function in the 1D coordinate space is expressed as

$$\left. \frac{d^2 f}{dz^2} \right|_{z_i} = \sum_{d=-\lambda}^{+\lambda} f(z_{i+d}) m_d^{(2)} \times (dz)^{-2}. \quad (\text{B2})$$

Using the matrix form of the Laplacian operator, together with the third local term in Eq. (B1), we have the kinetic matrix elements in the 1D FD representation

$$T_{ij} = -\frac{1}{2} [h^{1\text{D}}(z_i) + h^{1\text{D}}(z_j)] \nabla_{ij}^2 - [\nabla^2 h^{1\text{D}}(z)|_{z=z_i}] \delta_{ij}, \quad (\text{B3})$$

where $\nabla_{ij}^2 = m_d^{(2)} \times (dz)^{-2} \delta_{j,i+d}$, ($|d| \leq \lambda$) denotes the matrix elements for the Laplacian operator in the FD basis. The function $h^{1\text{D}}(z)$ is the 1D counterpart of $\frac{\hbar^2}{2m^*(\mathbf{r})}$ in Eq. (B1); dz is the spacing in the z direction.

2. Matrix elements in the 3D coordinate-space HO basis

The matrix elements in the 3D HO basis for the kinetic part (B1) are in the following form

$$\begin{aligned} \langle n_x n_y n_z | \hat{h}^{\text{kin}} | n'_x n'_y n'_z \rangle &= \int dx \int dy \int dz \psi_{n_x}^*(x) \psi_{n_y}^*(y) \psi_{n_z}^*(z) \hat{h} \psi_{n'_x}(x) \psi_{n'_y}(y) \psi_{n'_z}(z) \\ &= -\frac{1}{2} \int dx \int dy \int dz \psi_{n_x}^*(x) \psi_{n_y}^*(y) \psi_{n_z}^*(z) \frac{\hbar^2}{2m^*(\mathbf{r})} \nabla^2 [\psi_{n'_x}(x) \psi_{n'_y}(y) \psi_{n'_z}(z)] \\ &\quad - \frac{1}{2} \int dx \int dy \int dz \psi_{n_x}^*(x) \psi_{n_y}^*(y) \psi_{n_z}^*(z) \nabla^2 \left[\frac{\hbar^2}{2m^*(\mathbf{r})} \psi_{n'_x}(x) \psi_{n'_y}(y) \psi_{n'_z}(z) \right] \\ &\quad + \frac{1}{2} \int dx \int dy \int dz \psi_{n_x}^*(x) \psi_{n_y}^*(y) \psi_{n_z}^*(z) \left[\nabla^2 \frac{\hbar^2}{2m^*(\mathbf{r})} \right] \psi_{n'_x}(x) \psi_{n'_y}(y) \psi_{n'_z}(z), \end{aligned} \quad (\text{B4})$$

where $\psi_{n_\mu}(\mu)$ is the HO wave functions in the $\mu = x, y$, and z . The form of the Cartesian-coordinate HO basis $|n_x n_y n_z\rangle$ is identical to those explained in Ref. [34].

3. Matrix elements in the mixed basis

We write down the matrix elements in the mixed basis before a brief explanation of each term:

$$\begin{aligned}
\langle n_x n_y i_z | \hat{h}^{\text{kin.}} | n'_x n'_y i'_z \rangle &= -\frac{1}{2} \int dx \int dy \psi_{n_x}^*(x) \psi_{n_y}^*(y) \left[\frac{\hbar^2}{2m^*(x, y, z_{i_z})} \right] \left(\frac{d^2}{dx^2} + \frac{d^2}{dy^2} \right) [\psi_{n'_x}(x) \psi_{n'_y}(y)] \delta_{i_z, i'_z} (dz)^{-2} \\
&\quad -\frac{1}{2} \int dx \int dy \psi_{n_x}^*(x) \psi_{n_y}^*(y) \left(\frac{d^2}{dx^2} + \frac{d^2}{dy^2} \right) \left[\frac{\hbar^2}{2m^*(x, y, z_{i_z})} \psi_{n'_x}(x) \psi_{n'_y}(y) \right] \delta_{i_z, i'_z} (dz)^{-2} \\
&\quad -\frac{1}{2} \int dx \int dy \psi_{n_x}^*(x) \psi_{n_y}^*(y) \frac{1}{2} \left[\frac{\hbar^2}{2m^*(x, y, z_{i_z})} + \frac{\hbar^2}{2m^*(x, y, z_{i'_z})} \right] [\psi_{n'_x}(x) \psi_{n'_y}(y)] m_{i_z - i'_z}^{(2)} (dz)^{-2} \\
&\quad + \frac{1}{2} \int dx \int dy \psi_{n_x}^*(x) \psi_{n_y}^*(y) \left[\nabla^2 \frac{\hbar^2}{2m^*(\mathbf{r})} \right] \psi_{n'_x}(x) \psi_{n'_y}(y) \delta_{i_z, i'_z} (dz)^{-2}, \tag{B5}
\end{aligned}$$

where $|n_x n_y i_z\rangle$ is a 3D basis which uses the Cartesian coordinate HO bases $\psi_{n_x}(x)$ and $\psi_{n_y}(y)$ in the x and y directions, respectively. For the z direction, we use the FD basis, for which the ∇^2 and ∇ operators have been shown in Sec. B 1.

The first two terms in the right-hand side of Eq. (B5) correspond to the first two terms in Eq. (B1) for the x and y directions. In these two terms, the matrix is diagonal in the z -direction, due to the local property. The third term corresponds to the first two terms in Eq. (B1) for the z direction. It has been symmetrized in the same way as explained in Sec. B 1. The coefficients $m_{i_z - i'_z}^{(2)}$ are non-zero only for $|i_z - i'_z| \leq \lambda$. The last term corresponds to the last term in Eq. (B1). It is diagonal for the basis index in the z direction due to its locality.

Appendix C: The SO terms in various basis

For the SO term, the matrix form can be obtained in a very similar way. The SO part of the Hamiltonian reads

$$-i \left(\begin{array}{c} \frac{\partial f(\mathbf{r})}{\partial x} \frac{\partial}{\partial y} - \frac{\partial f(\mathbf{r})}{\partial y} \frac{\partial}{\partial x} \\ \left[\frac{\partial f(\mathbf{r})}{\partial y} \frac{\partial}{\partial z} - \frac{\partial f(\mathbf{r})}{\partial z} \frac{\partial}{\partial y} \right] + i \left[\frac{\partial f(\mathbf{r})}{\partial z} \frac{\partial}{\partial x} - \frac{\partial f(\mathbf{r})}{\partial x} \frac{\partial}{\partial z} \right] \end{array} \left[\frac{\partial f(\mathbf{r})}{\partial y} \frac{\partial}{\partial z} - \frac{\partial f(\mathbf{r})}{\partial z} \frac{\partial}{\partial y} \right] - i \left[\frac{\partial f(\mathbf{r})}{\partial z} \frac{\partial}{\partial x} - \frac{\partial f(\mathbf{r})}{\partial x} \frac{\partial}{\partial z} \right] \right),$$

where $f(\mathbf{r}) \equiv b_4 \rho(\mathbf{r}) - b'_4 \rho_q(\mathbf{r})$ is a scalar function of position.

Next, we list the two typical terms in the SO term: $\frac{\partial f(\mathbf{r})}{\partial x} \frac{\partial}{\partial y}$ and $\frac{\partial f(\mathbf{r})}{\partial y} \frac{\partial}{\partial z}$, which contain operators with and without derivative in the z direction:

$$\langle n_x n_y i_z | \frac{\partial f(\mathbf{r})}{\partial x} \frac{\partial}{\partial y} | n'_x n'_y i'_z \rangle = \int dx \int dy \psi_{n_x}^*(x) \psi_{n_y}^*(y) \frac{\partial f(\mathbf{r})}{\partial x} \psi_{n'_x}(x) \frac{d\psi_{n'_y}(y)}{dy} \delta_{i_z, i'_z}, \tag{C1}$$

$$\langle n_x n_y i_z | \frac{\partial f(\mathbf{r})}{\partial y} \frac{\partial}{\partial z} | n'_x n'_y i'_z \rangle = \int dx \int dy \psi_{n_x}^*(x) \psi_{n_y}^*(y) \frac{\partial f(\mathbf{r})}{\partial y} \psi_{n'_x}(x) \psi_{n'_y}(y) m_{i'_z - i_z}^{(1)} (dz)^{-1}. \tag{C2}$$

-
- [1] T. Nakatsukasa, K. Matsuyanagi, M. Matsuo, and K. Yabana, *Rev. Mod. Phys.* **88**, 045004 (2016).
[2] P. Ring and P. Schuck, *The Nuclear Many-Body Problem* (Springer-Verlag, Berlin, 1980).
[3] M. Brack, J. Damgaard, A. S. Jensen, H. C. Pauli, V. M. Strutinsky, and C. Y. Wong, *Rev. Mod. Phys.* **44**, 320 (1972).
[4] M. Bender, P.-H. Heenen, and P.-G. Reinhard, *Rev. Mod. Phys.* **75**, 121 (2003).
[5] D. Vautherin and D. M. Brink, *Phys. Rev. C* **5**, 626 (1972).
[6] J. Dobaczewski, H. Flocard, and J. Treiner, *Nucl. Phys. A* **422**, 103 (1984).
[7] D. Gogny, *Nucl. Phys. A* **237**, 399 (1975).
[8] J. Dechargé and D. Gogny, *Phys. Rev. C* **21**, 1568 (1980).
[9] W. Younes and D. Gogny, *Phys. Rev. C* **80**, 054313 (2009).
[10] B. D. Serot and J. D. Walecka, *Relativistic nuclear many-body theory*, in *Recent Progress in Many-Body Theories: Volume 3*, edited by T. L. Ainsworth, C. E. Campbell, B. E. Clements, and E. Krotschek (Springer US, 1992) pp. 49–92.
[11] P. Ring, *Prog. Part. Nucl. Phys.* **37**, 193 (1996).
[12] J. Meng, H. Toki, S. Zhou, S. Zhang, W. Long, and L. Geng, *Prog. Part. Nucl. Phys.* **57**, 470 (2006).

- [13] S. Shen, H. Liang, W. H. Long, J. Meng, and P. Ring, *Prog. Part. Nucl. Phys.* **109**, 103713 (2019).
- [14] P. Bonche, H. Flocard, P. Heenen, S. Krieger, and M. Weiss, *Nucl. Phys. A* **443**, 39 (1985).
- [15] J. C. Pei, G. I. Fann, R. J. Harrison, W. Nazarewicz, Y. Shi, and S. Thornton, *Phys. Rev. C* **90**, 024317 (2014).
- [16] S. Jin, A. Bulgac, K. Roche, and G. Wlazłowski, *Phys. Rev. C* **95**, 044302 (2017).
- [17] Y. Kashiwaba and T. Nakatsukasa, *Phys. Rev. C* **100**, 035804 (2019).
- [18] M. Yamagami, *Phys. Rev. C* **100**, 054302 (2019).
- [19] K. Bennaceur and J. Dobaczewski, *Comput. Phys. Commun.* **168**, 96 (2005).
- [20] W. Pöschl, D. Vretenar, and P. Ring, *Comp. Phys. Commun.* **103**, 217 (1997).
- [21] E. Terán, V. E. Oberacker, and A. S. Umar, *Phys. Rev. C* **67**, 064314 (2003).
- [22] J. C. Pei, M. V. Stoitsov, G. I. Fann, W. Nazarewicz, N. Schunck, and F. R. Xu, *Phys. Rev. C* **78**, 064306 (2008).
- [23] K. Yoshida and N. V. Giai, *Phys. Rev. C* **78**, 064316 (2008).
- [24] D. G. Ravenhall, C. J. Pethick, and J. R. Wilson, *Phys. Rev. Lett.* **50**, 2066 (1983).
- [25] M. Hashimoto, H. Seki, and M. Yamada, *Prog. Theor. Phys.* **71**, 320 (1984).
- [26] P. Magierski and P.-H. Heenen, *Phys. Rev. C* **65**, 045804 (2002).
- [27] W. G. Newton and J. R. Stone, *Phys. Rev. C* **79**, 055801 (2009).
- [28] B. Schuetrumpf and W. Nazarewicz, *Phys. Rev. C* **92**, 045806 (2015).
- [29] Y. Hashimoto, *Eur. Phys. J. A* **48**, 55 (2012).
- [30] Y. Hashimoto, *Phys. Rev. C* **88**, 034307 (2013).
- [31] J. Dobaczewski, W. Satuła, B. Carlsson, J. Engel, P. Olbratowski, P. Powałowski, M. Sadziak, J. Sarich, N. Schunck, A. Staszczak, M. Stoitsov, M. Zalewski, and H. Zduńczuk, *Comput. Phys. Commun.* **180**, 2361 (2009).
- [32] Y. Shi, *Phys. Rev. C* **98**, 014329 (2018).
- [33] W. Ryssens, V. Hellemans, M. Bender, and P.-H. Heenen, *Comput. Phys. Commun.* **187**, 175 (2015).
- [34] J. Dobaczewski and J. Dudek, *Comput. Phys. Commun.* **102**, 166 (1997).
- [35] Y. Shi, N. Hinohara, and B. Schuetrumpf, *Phys. Rev. C* **102**, 044325 (2020).
- [36] J. Bartel, P. Quentin, M. Brack, C. Guet, and H.-B. Håkansson, *Nucl. Phys. A* **386**, 79 (1982).
- [37] N. Schunck, D. Duke, H. Carr, and A. Knoll, *Phys. Rev. C* **90**, 054305 (2014).
- [38] J. Dobaczewski and J. Dudek, *Comput. Phys. Commun.* **102**, 166 (1997).